Ultra-thin defective TiO_2 films as photocathodes for selective CO_2 reduction to formate

Amiri, Mahsa; Ahmadi, Majid; Khossossi, Nabil; Gonugunta, Prasad; Roohi, Khatereh; Kooi, Bart; Ramdin, Mahinder; Anusuyadevi, Prasaanth Ravi; Tätte, Tanel; Kongi, Nadezda

DOI
10.1016/j.jcat.2025.116022

Publication date
2025

Document Version
Final published version

Published in
Journal of Catalysis

Citation (APA)
Amiri, M., Ahmadi, M., Khossossi, N., Gonugunta, P., Roohi, K., Kooi, B., Ramdin, M., Anusuyadevi, P. R., Tätte, T., Kongi, N., Vanetsev, A., Dey, P., & Taheri, P. (2025). Ultra-thin defective TiO_2 films as photocathodes for selective CO_2 reduction to formate. *Journal of Catalysis*, *445*, Article 116022. https://doi.org/10.1016/j.jcat.2025.116022

Journal of Catalysis 445 (2025) 116022

Contents lists available at ScienceDirect

Journal of Catalysis

journal homepage: www.elsevier.com/locate/jcat

Research article

Ultra-thin defective TiO_2 films as photocathodes for selective CO_2 reduction to formate

Mahsa Amiri [a], Majid Ahmadi [b], Nabil Khossossi [c], Prasad Gonugunta [c], Khatereh Roohi [c], Bart Kooi [b], Mahinder Ramdin [d], Prasaanth Ravi Anusuyadevi [c], Tanel Tätte [a], Nadezda Kongi [e,*], Alexander Vanetsev [a,*], Poulumi Dey [c], Peyman Taheri [c]

[a] Institute of Physics, University of Tartu, Ostwaldi 1, 50411 Tartu, Estonia
[b] Zernike Institute for Advanced Materials, Faculty of Science and Engineering, University of Groningen, 4 Nijenborgh, 9747 AG Groningen, the Netherlands
[c] Department Materials Science and Engineering (MSE), Faculty of Mechanical Engineering (ME), Delft University of Technology, Mekelweg 2, 2628 CD Delft, the Netherlands
[d] Engineering Thermodynamics, Process & Energy Department, Faculty of Mechanical Engineering, Delft University of Technology, Leeghwaterstraat 39, 2628 CB Delft, the Netherlands
[e] Institute of Chemistry, University of Tartu, Ravila 14a, 50411 Tartu, Estonia

ARTICLE INFO

Keywords:
CO_2 reduction
Photo-electrochemistry
Ultra-thin defective films
Anatase
Sol-gel

ABSTRACT

Titanium dioxide (TiO_2) has been widely used as a photocatalyst in CO_2 reduction reaction (CO_2RR) due to its low cost, high stability, and strong absorption in the close-to-visible ultra-violet (UV) range. However, TiO_2 films suffer from poor selectivity in CO_2 reduction due to their unfavorable electronic properties. In this work, we address this challenge by fabricating ultra-thin (14 nm) defective TiO_2 films (TiO_2-DTF) to enhance the selectivity of CO_2RR towards formate.

TiO_2 sol was prepared using a facile and reproducible sol-gel method and directly deposited onto the surface of the electrode, forming a uniform, ultra-thin TiO_2 layers with a high number of defects. The activity of the TiO_2-DTF catalyst was studied in both photochemical and photoelectrochemical CO_2RR, indicating that the applied potential increases both the yield and selectivity of CO_2RR to formate. The TiO_2-DTF photocathode exhibited remarkable formate production during CO_2 reduction, achieving exceptional Faradaic efficiencies of up to 45 %. To elucidate the mechanism of photoelectrochemical CO_2RR on TiO_2-DTF, an *in-situ* attenuated total reflection Fourier-transform infrared spectroscopy (*in-situ* ATR-FTIR) was used and experimental results were supported by density functional theory (DFT) calculations. This study demonstrates that ultra-thin highly defective TiO_2 film, prepared using the cost-effective and environmentally friendly sol-gel method, can be used as photo-electrocatalyst for CO_2 reduction.

1. Introduction

The problem of carbon dioxide (CO_2) emissions from fossil-based fuels and the related issue of CO_2 conversion represent significant environmental concerns [1,2]. Efforts to mitigate this impact include capturing, storing, and converting CO_2 into valuable products [3,4]. Converting CO_2 to fuels attracts substantial attention as a green process contributing to the carbon–neutral energy cycle [5–9]. CO_2 reduction can be performed by several methods, including thermochemical, photocatalytic, electrochemical, photoelectrochemical, and biochemical processes [10]. Among various CO_2 conversion products [10], formic acid has gained a significant interest due to its unique properties [11–13]. As a stable liquid with low toxicity, formic acid serves as an advantageous and versatile compound, finding applications not only as a chemical building block, but also as a potential hydrogen storage matrix, avoiding challenges associated with hydrogen handling, storage, and transportation [11,14].

In recent years, photocatalytic and electrochemical approaches have gained a greater attention, as they offer the possibility of storing intermittent renewable energy [15,16]. The conversion of CO_2 via photocatalysis (PC) is widely recognized as one of the most promising approaches [6,17]. Nonetheless, photocatalysis exhibits notably low

* Corresponding authors.
E-mail addresses: nadezda.kongi@ut.ee (N. Kongi), alexander.vanetsev@ut.ee (A. Vanetsev).

https://doi.org/10.1016/j.jcat.2025.116022
Received 14 September 2024; Received in revised form 19 January 2025; Accepted 12 February 2025
Available online 15 February 2025

energy efficiency due to its inherent bottleneck of low solar photon utilization (especially in the visible and IR region) coupled with short lifetime of photogenerated charges and high recombination rate [18,19]. Consequently, the emergence of photoelectrocatalysis (PEC) is gaining prominence due to its potential to combine the efficient charge generation by photoexcitation and enhanced proton electron transfer by applied potential [10,20,21]. In PEC system, an external circuit separates photogenerated charges towards their respective electrodes, minimizing recombination rates. For instance, in a photocathode-driven PEC system, light induces electron-hole pairs at the cathode. Due to a voltage bias, holes migrate to the anode, initiating oxidation reactions, while electrons on the photocathode surface drive reduction reactions [22].

Since the beginning of PEC studies, titanium dioxide (TiO_2) has been a focal point among semiconductor materials, owing to its high density of photogenerated charges and stability under harsh conditions [23–26]. However, its low conductivity, insufficient visible light absorption and fast recombination rate constrain its potential for utilization in photoelectrochemical applications [22]. To design efficient TiO_2-based catalysts for the photoelectrochemical CO_2 reduction reaction (CO_2RR), it is important to address these drawbacks. Several approaches have been used in the recent times, like defect engineering, doping, hybridization, and control of textural properties, to eliminate the above limitations associated with catalytic-TiO_2 systems [22]. Moreover, understanding the dynamic process and reaction mechanisms involved remains a challenging task due to various factors influencing efficiency and selectivity. For example, TiO_2 nanowire/graphite fiber hybrid photocatalysts have been used as a high performing water splitting materials for hydrogen generation [27]. High performance originated from the presence of heterostructures between the semiconductor TiO_2 nanowires with highly photoactive facet (1 1 0) exposed to the solution and the zero-bandgap graphite fibers. In another work, a combination of p-type Cu_2O and n-type TiO_2 allowed to construct a stable and efficient heterojunction photocathode for water splitting [28]. InP and SnO_2 were assembled onto TiO_2 nanotubes (NTs) in two different orders, resulting in InP/SnO_2/TiO_2 NTs and SnO_2/InP/TiO_2 NTs. The SnO_2/InP/TiO_2 NTs exhibited a lower energy band gap (2.96 eV) compared to InP/SnO_2/TiO_2 NTs (3.15 eV) and superior performance in CO_2RR to methanol. The use of TiO_2 nanotubes in this configuration likely contributed to improved charge transfer and enhanced photoelectrocatalytic performance, making it a crucial component in achieving the observed efficiency and selectivity in the photoelectrocatalytic process [29]. Recently, TiO_2 nanowire/graphite sheet hybrid covalently modified by eosin dye has demonstrated efficient photoelectrocatalytic reduction of CO_2, yielding ethanol as the primary product [30]. TiO_2 in various hybrid configurations, involving co-catalysts, multi-semiconductor systems, and nanostructures has recently been reviewed as a promising catalyst for the photoelectrochemical reduction of CO_2 to methanol [31]. However, high catalytic efficiency is mainly achieved through increased complexity of the catalyst system, which is not sustainable at a large scale due to high price and complicated synthetic procedures. To progress from complex TiO_2-based hybrid structures, a shift towards simplicity, sustainability, and cost-effectiveness is necessary for CO_2 photoelectrocatalysis. Thin film-based catalysts enhance electronic properties by reducing electron-hole recombinations [32,33], while the durability of an intact, uniform ultra-thin layer of catalyst is anticipated to surpass that of binder-bound nanoparticles. Moreover, the scalability of this simple process offers a practical pathway for large-scale implementation while maintaining efficient catalytic performance.

This study demonstrates the use of highly defective ultrathin TiO_2 films (TiO_2-DTF), offering a novel solution to the known drawbacks of bulk TiO_2 (nano)structures. High concentration of defects is achieved through formation of oxygen vacancies and Ti^{3+} surface defects (TSD). TSDs are produced from the reduction of Ti^{4+} to Ti^{3+} as a charge compensation mechanism [34]. The latter mechanism plays a deciding role in the formation of defects during thermal treatment of amorphous TiO_2. Highly defective TiO_2 films, consisting of both anatase and amorphous phases are likely to have enhanced photoelectrochemical efficiency due to high concentration of active sites promoting charge transfer processes [35].

Utilization of TiO_2-DTF improves charge transfer processes, making CO_2 photoelectroreduction more efficient while maintaining a sustainable, inexpensive, and scalable catalyst design. The thickness of the film is a crucial parameter influencing photoelectron conversion efficiency [36]. Additionally, the presence of defects in the structure can significantly enhance photoelectrohemical conversion efficiency by providing active sites for CO_2 adsorption, altering the electronic structure and band gap, and thereby increasing light absorption across a broader solar spectrum [37–39]. Selection of ultra-thin TiO_2 films is driven by its advantages, including a larger surface area, accelerated electron-hole separation, reduced recombination, higher number of exposed surface metal atoms, and an increased density of defective sites. For a comprehensive understanding of the CO_2 photoelectroreduction mechanism, density functional theory (DFT) modeling was performed.

2. Results and discussion

2.1. Preparation and structural characterization of TiO_2-DTF photocathode

In this work, TiO_2 films with two different thicknesses (14 and 30 nm) were prepared, referred as “thin film” and “thick film” hereafter. The titania sol precursor was synthesized using the sol-gel method, employing titanium butoxide as the precursor and acetic acid as a polycondensation rate-controlling agent [40]. The concentration of the sol precursor was adjusted to control the thickness of the prepared films (see experimental details in Supporting Information). For thin films, a 1:36 ratio of titanium butoxide to 1-butanol optimized the sol viscosity for producing ultra-thin layers (~14 nm) during spin-coating, while a 1:18 ratio resulted in thicker films (~30 nm).

The sol-gel method offers distinct advantages over conventional powder-based approaches for preparing TiO_2 materials. It enables precise control over film thickness, uniformity and defect density of the TiO_2 thin films. Achieving high level of control over uniformity is challenging with powders, which often require additional processing steps such as pressing or sintering to form a coherent structure. Furthermore, the direct deposition of sol-gel-derived films onto substrates eliminates the need for binders or adhesives, reducing the risk of contamination and ensuring better contact between TiO_2 thin films and the electrode surface.

Unlike conventional sol-gel methods, the synthesis process in this study avoided the direct addition of water. Instead, the water required for hydrolysis was gradually generated *in-situ* via an esterification reaction between acetic acid and butanol. This approach enabled precise control over the hydrolysis rate of titanium butoxide, minimizing rapid precipitation or particle agglomeration.

TiO_2-DTF photocathodes were prepared by direct deposition of titania sol onto glassy carbon (GC) electrode by spin-coating with subsequent thermal treatment at 550 °C. GC support was chosen due to its high electrical conductivity, chemical stability, and inert electrochemical nature, which allows to focus on the intrinsic properties of the TiO_2 film without interference from the substrate.

High-resolution transmission electron microscopy (HRTEM) was used to analyze the composition and crystalline structure of the prepared TiO_2-DTF (Fig. 1a,c for thin film and S3b for thick film).

As shown in Fig. 1a,b, the thin film is composed of spheroidal grains with a diameter in the range of 10–15 nm and is characterized by an average thickness of 14 nm. Multiple measurements of interplanar distances of several randomly selected crystallites (red, green and blue boxes) resulted in one characteristic distance of 3.52 ± 0.05 Å, which corresponds to the (1 0 1) plane of TiO_2 anatase phase. No characteristic interatomic distances, corresponding to rutile or any other crystalline

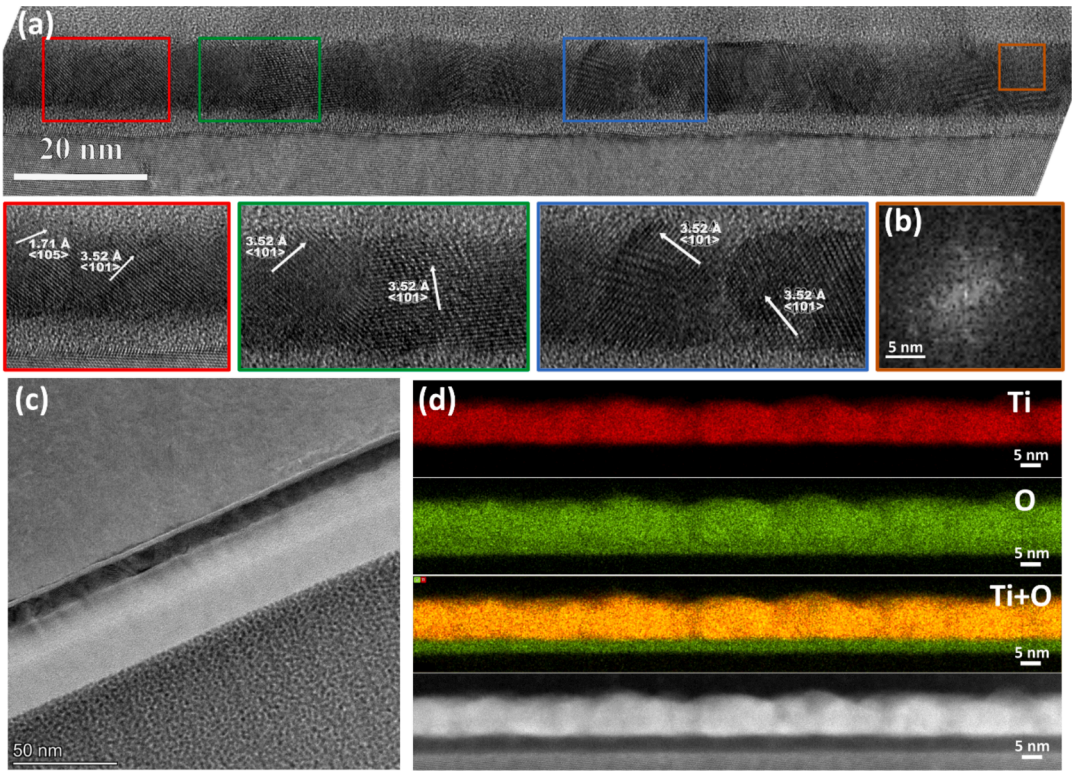

Fig. 1. HRTEM image recorded from the synthesized TiO_2-DTF: (a) cross-section of the TiO_2-DTF with magnified specific regions; (b) FFT pattern of the selected region with lower crystallinity; (c) out-of-plane view of TiO_2-DTF; (d) cross-sectional O, Ti, and overlap of Ti and O elemental mapping for the TiO_2-DTF and relative HAADF STEM image.

phases of TiO_2 were discernible, leading to the assumption that synthesized TiO_2 films is predominantly comprised of the anatase phase. In comparison, thick film has an average thickness of 30 nm and consists of anatase with inclusions of an amorphous phase, according to HRTEM analysis (Fig. S3b). Magnified regions of the cross-section show the reduced material density, potentially indicative of film porosity, better visible on SEM images (Fig. S3c). This porosity may be attributed to the synthesis conditions (evolution of gaseous products during drying) or subsequent post-processing procedures [41,42]. The presence of potential amorphous inclusions is marked by the orange box in the HRTEM image.

Fast Fourier transform (FFT) analysis further verified a lower degree of crystallinity in this specific region, as illustrated in Fig. 1b. Elemental mapping of the TiO_2-DTF cross-section is shown in Fig. 1d, indicating uniform distribution of Ti and O elements within the thin film.

To examine chemistry and the presence of defects on the TiO_2 films (both thick and thin) surface, X-ray photoelectron spectroscopy (XPS) measurements were conducted. XPS survey spectra (Fig. S4), reveals characteristic binding energy peaks for Ti, O, and C elements on both, thin and thick films, respectively. While Ti2p and O1s peaks are prominent, the intense C1s peak likely arises from the large surface area exposure to ambient air and formation of carbon contamination. Fig. 2a and b show high-resolution spectra of Ti2p levels of thin and thick films, respectively. Distinctive doublet peaks in these spectra are originating from the spin orbital splitting of photoelectrons corresponding to $Ti2p_{3/2}$ and $Ti2p_{1/2}$ core levels. For the thin film, binding energies are observed at 458.29 eV for $Ti2p_{3/2}$ and 464.07 eV for $Ti2p_{1/2}$, while the thick film exhibits peaks at 458.22 eV and 463.96 eV, respectively [43]. In anatase, the presence of titanium in the oxidation state of +4 is associated with a binding energy difference $\Delta E_b = E_b(Ti2p_{1/2}) - E_b(Ti2p_{3/2})$, which is equal to 5.7 eV [44,45]. However, deviations to 5.78 eV and 5.72 eV for thin and thick films suggest the presence of both Ti^{4+} and Ti^{3+} TSD states, likely due to oxygen vacancy-induced charge compensation. Peak deconvolution indicates a prevalence of defects in the thin film, as evidenced by the prominent Ti^{3+} defect-related peak at ~457.85 eV and the Ti-O lattice peak at 458.65 eV. Conversely, the diminished intensity and area of the ~457.47 eV peak in the thick film imply a lower proportion of Ti^{3+} states (areas of 6356 vs. 3308, as shown in Table 1).

The O1s spectra (Fig. 2c and d) have been deconvoluted into three distinct peaks occurring at approximately 533 eV, 531.5 eV, and 529.7 eV. These peaks are ascribed to adsorbed oxygen-containing species, oxygen vacancies, and lattice oxygen within the TiO_2 matrix, respectively [45–49]. Typically, the elevation of the electronic state is attained by introducing co-catalysts through the doping of TiO_2 [50]. In this work, the creation of Ti^{3+} defects and oxygen vacancies in TiO_2-DTF is achieved by employing an optimized synthetic technique. The concentration of oxygen vacancies is higher for thin film as indicated by large area under corresponding peak (6910 vs. 4978, as shown in Table 1).

A higher intensity of Ti^{3+} peaks in thinner films indicates a greater density of oxygen vacancies (O_v) and associated defects (Table 1). This is attributed to the more rapid solvent evaporation and reduced material density during annealing in thinner films. The disparity in defect density between thin and thick films can be explained by differences in film thickness, and precursor distribution during the sol-gel synthesis process. The thinner 14 nm film exhibits a higher defect density due to its reduced material volume, which enhances oxygen diffusion during the annealing step and promotes the formation of O_v and Ti^{3+} sites. The higher surface-to-volume ratio in thinner films further facilitates defect formation at both surface and subsurface levels, contributing to increased oxygen mobility. In contrast, the thicker 30 nm film, with a larger material volume, exhibits a lower defect density. Limited oxygen diffusion across the thicker structure during annealing, combined with slower diffusion kinetics and a more constrained lattice environment, inhibits the formation of O_v and Ti^{3+} defects. Moreover, the thicker film may experience greater thermal stress during annealing, leading to partial defect annealing or fewer defects forming overall. The higher

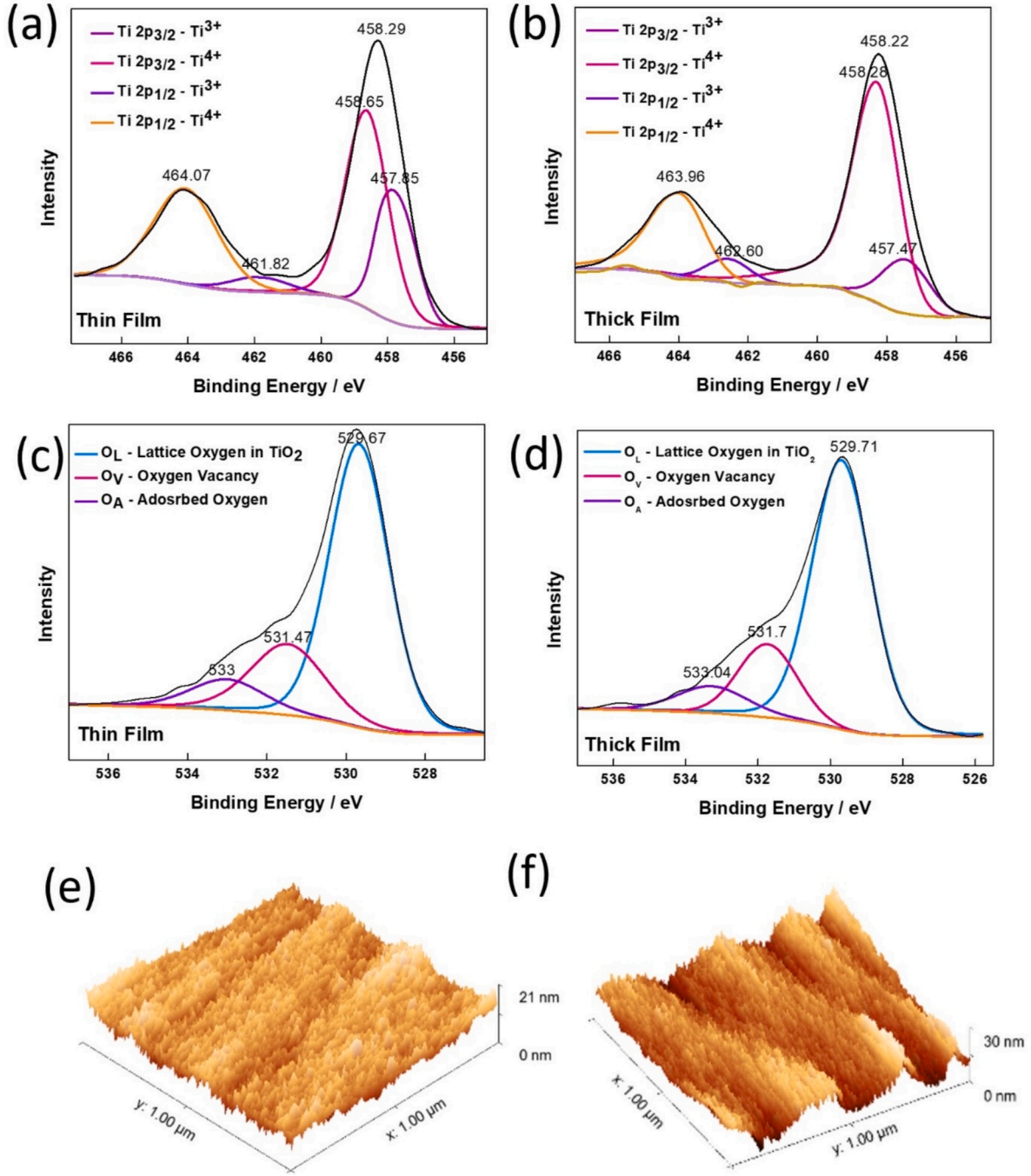

Fig. 2. High-resolution narrow scan spectra of (a-b) Ti2p, and (c-d) O1s levels; (e-f) AFM nanoscale topography of thin and thick TiO_2 films, respectively.

Table 1
Comparative analysis of O1s and Ti2p core level peaks for thin and thick TiO_2 films.

Thin film	**Ti2p**	Position	457.68	458.62	461.82	464.07
		Area	6356	11,241	1167	8006
	O1s	Position	529.67	531.47	533.00	
		Area	20,819	6910	3006	
Thick film	**Ti2p**	Position	457.47	458.28	462.60	463.96
		Area	3308	14,799	1324	6478
	O1s	Position	529.71	531.70	533.04	
		Area	22,518	4978	3624	

defect density in the thinner film directly correlates with its enhanced photocatalytic activity, as defects such as Ti^{3+} and Ov serve as active sites for CO_2 adsorption and reduction. Please note that the defect density increases approximately in proportion to the film thickness (30/14 ≈ 2, Ti^{3+}: 6356 vs. 3308 ≈ 2).

The surface topography of both thin and thick TiO_2 films was analyzed using atomic force microscopy (AFM) technique. The AFM images in Fig. 2e and f provide a detailed view of the surface roughness and waviness of the TiO_2 films measured on an area of 1 μm^2. The surface of as-fabricated TiO_2-DTF exhibit a very low root-mean-square (RMS) roughness of about 1.8 nm (thin film) and 4.9 nm (thick film). Achieving an optimal balance in coating thickness and surface area is crucial for maintaining an effective photocatalytic activity, as excessive thickness may lead to a promotion of the charge recombination process

[51,52], while increased roughness positively influences surface reactions [53–56].

2.2. Photoelectrochemical CO_2RR in potassium bicarbonate solution

2.2.1. Photoelectrochemical characterization of TiO_2-DTF samples

To evaluate the electrical properties of the prepared TiO_2-DTF samples, electrochemical impedance spectroscopy (EIS) was conducted under both dark and illuminated conditions (Fig. 3a, b). In the dark, both films exhibited high resistance in the range of $\sim 10^6$ Ω due to limited charge carrier density (Fig. 3a). The thin film showed slightly higher resistance compared to the thick film, attributed to its higher defect density. Upon UV illumination, a significant reduction in resistance was observed in both films, demonstrating the photoconductive nature of the TiO_2-DTF samples (Fig. 3b).

Notably, the thin film exhibited a much lower charge transfer resistance than its thicker counterpart under UV light (4.3×10^4 Ω vs. 0.33×10^6 Ω). Upon UV illumination, the thin film demonstrates a drastic reduction in resistance, indicating the generation of photo-induced charge carriers. This pronounced reduction highlights the generation of photo-induced charge carriers in the thin film, which effectively suppresses charge recombination and facilitates electron transfer to adsorbed CO_2 molecules. The enhanced photoconductivity observed in the thin film directly correlates with its superior photocatalytic efficiency. The Nyquist plots further confirm the critical role of UV light in activating charge carriers and improving overall catalytic performance.

This reduction in charge carrier recombination rate is critical as it directly correlates with the improved photoactivity and efficiency of the catalytic process. Consequently, only the 14 nm thin TiO_2 film was further studied as the photocathode.

Linear sweep voltammetry (LSV) experiments were performed on the 14 nm TiO_2-DTF sample under both dark and UV light-illuminated conditions in a CO_2-saturated 0.1 M $KHCO_3$ electrolyte (Fig. 3c). The LSV curves demonstrate a significant enhancement in catalytic activity upon UV illumination. Under dark conditions, the current density at −1.4 V is limited to −40 mA cm^{-2}, whereas UV light increases it substantially to −65 mA cm^{-2}.

This pronounced increase highlights the critical role of light activation in improving charge separation and facilitating efficient electron transfer to adsorbed CO_2 molecules. The results confirm that UV illumination enhances the photoelectrochemical properties of the thin TiO_2-DTF sample, driving the reduction of CO_2 with greater efficiency.

This result indicates that application of UV light enhances the catalytic properties of the TiO_2-DTF. LSV curves illustrate the role of light in enhancing catalytic activity. The LSV curve obtained for the 14 nm TiO_2-DFT sample under UV light resembles a photoelectrolysis process [26]. This behavior suggests that while the electrochemical processes are consistent, UV light activates the photoelectrocatalytic properties. This substantial increase confirms that light activation improves charge separation, enabling efficient electron transfer to CO_2 molecules and subsequent reduction of CO_2. EIS data supports this, showing a drastic reduction in charge transfer resistance for the thin film under light compared to the thick film, highlighting improved photoconductivity.

While the LSV curves intend to exhibit differences in current density in the presence of light, a higher theoretical photovoltage is expected for TiO_2 under ideal conditions. This discrepancy could be attributed to the TiO_2 deposited on the glassy carbon, where the interface between the two materials imposes contact issues. In line with the following information: poor ohmic contacts between the TiO_2 and the electrodes can lead to increased resistance and voltage drops, thereby reducing the photovoltage. Additionally, possible Schottky barriers at the contacts may impede charge collection and further diminish the effective photovoltage.

Photoelectrochemical stability of the fabricated TiO_2-DTF was further investigated using chronoamperometry (CA) at various potentials under UV light. The electrode demonstrated sustained stability throughout the 1-hour test at different potentials (Fig. S1). The obtained LSV data was further used for the determination of Faradaic efficiency of the TiO_2-DTF during CO_2 photoelectroreduction.

2.2.2. Analysis of CO_2 photoelectroreduction reaction products

Analysis of gaseous products was performed in a photoelectrochemical cell (Fig. 3d) coupled with a potentiostat and gas

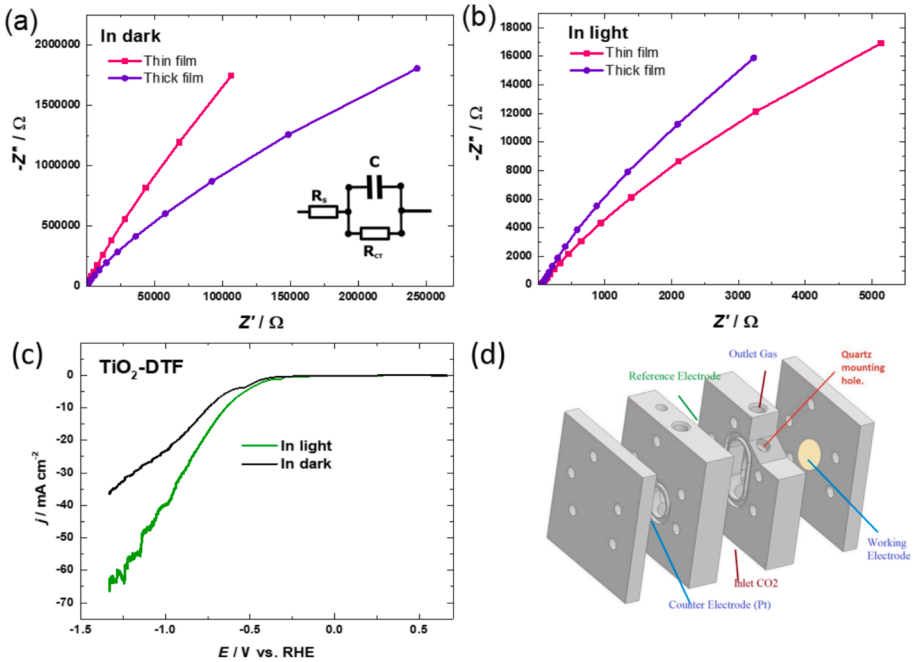

Fig. 3. (a, b) Nyquist plots obtained for both TiO_2-DTF samples in dark and light conditions, respectively; (c) LSV curves obtained for 14 nm TiO_2-DTF sample in the dark (black line) and under UV light (green line); (d) photoelectrochemical cell. (For interpretation of the references to colour in this figure legend, the reader is referred to the web version of this article.)

chromatograph (GC), described in SI. Liquid products in the electrolyte were sampled from the cell and analyzed using high-performance liquid chromatography (HPLC). The main products of CO_2RR on TiO_2-DTF are shown in Fig. 4 and yields are summarized in Table S2. Following a 50-min exposure to UV irradiation, formate, carbon monoxide, and methane were detected. Before the application of potential, formate becomes the main product of CO_2 reduction, while methane and CO are generated in much lower quantities. The extension of UV-irradiation duration only results in a slight increase in product yields. The application of potential results in increased yields for all products, with formate exhibiting the highest production yield. The maximum Faradaic efficiency (Table S3) of formate production −45 %, was achieved at −1.2 V and current density of 5.26 mA cm^{-2}, indicating that further increase of potential is less efficient for the energy-to-product conversion, though yield of the formate continued to increase. The Faradaic efficiency decreases due to the competitive production of hydrogen (see Table S3), a common occurrence on the TiO_2 surfaces in aqueous media [57,58]. The generation of H_2 is less critical when the desired product is formate, as, unlike CO, formate remains in liquid phase and therefore is easily separable from CO, H_2 and CH_4 byproducts.

The 30 nm TiO_2 film (refer to Table S3) displayed a Faradaic efficiency of only 15 %, emphasizing the crucial role of optimizing film thickness in governing recombination and charge transfer processes. Lowering film thickness enhances charge transfer, reducing the probability of charge recombination, thereby improving catalytic performance and selectivity.

Determining the absolute yield per a specific amount of catalyst is crucial for the practical application of CO_2 photoelectroreduction. In this study, the absolute yields were calculated per square centimeter of the catalyst surface, a choice dictated by the specific characteristics of TiO_2-DTF. This methodology complicates direct comparisons with state-of-the-art, as yields are often expressed per gram of catalyst. Due to the extreme thinness of TiO_2-DTF layer, it yields substantial values, ranging from 1 to 5 mol $h^{-1}g^{-1}$. However, the more practically significant metric is the yield per square centimeter, as the feasibility of an industrial process relies on the yield per surface of catalyst. Thus, we used only the highest values of Faradaic efficiency to compare our results with the state-of-the-art.

Recent studies have shown advancements in CO_2 conversion to formate on different photocathodes [59]. Liu et al. proposed novel photocathode composed of sensitized cuprous oxide (p-nCu_2O) on hydroxyl iron oxide (FeOOH) enhanced with cobalt-doped cadmium sulfide (Co:CdS) quantum dots. This photocathode achieved high photovoltage and selective CO_2 reduction, yielding formic acid with up to 82.9 % Faradaic efficiency at −0.8 V vs. RHE [60]. Dong et al. reported CuS/GaN/Si photocathode with Faradaic efficiency of HCOOH = 70.2 % at −1.0 V vs. RHE under 100 mW cm^{-2} artificial sun illumination [61]. Rao et al. demonstrated the utilization of high-quality Si photocathodes decorated with Sn porous nanowire catalysts, achieving a formate FE of 59.2 % at −0.4 V vs. RHE under simulated sunlight at an intensity of 100 mW cm^{-2} [61]. Promising results were achieved by Yanguang Li et al. who used arrays of defective bismuth nanotubes on Si substrate to conduct efficient PEC conversion of CO_2 into formate with 95 % Faradaic efficiency at −0.4 V vs. RHE under simulated sunlight at an intensity of 50 mW cm^{-2} [62]. Tin nanoparticles on aligned Si wires allowed to achieve ~40 % Faradaic efficiency for formate production at −0.875 V vs. RHE under artificial sunlight with intensity of 100 mW cm^{-2} [63]. GaN:Sn nanohybrids exhibited Faradaic efficiency of 77 % towards formate at −0.53 V vs. RHE under simulated sunlight at an intensity of 100 mW cm^{-2} [64]. TiO_2/Si photocathode with electrodeposited tin nanostructures exhibited maximum FE of 69 % towards formate at −1 V vs. RHE under artificial sunlight with intensity of 100 mW cm^{-2} [65]. All previous studies are mostly focusing on heavy metal-based nanostructure. In contrast, this work employs TiO_2 without co-catalyst, unusual for formate production but simpler and more versatile also demonstrating the conversion mechanism. It is important to note that while most published results are conducted using simulated sunlight, our study employs intense UV radiation.

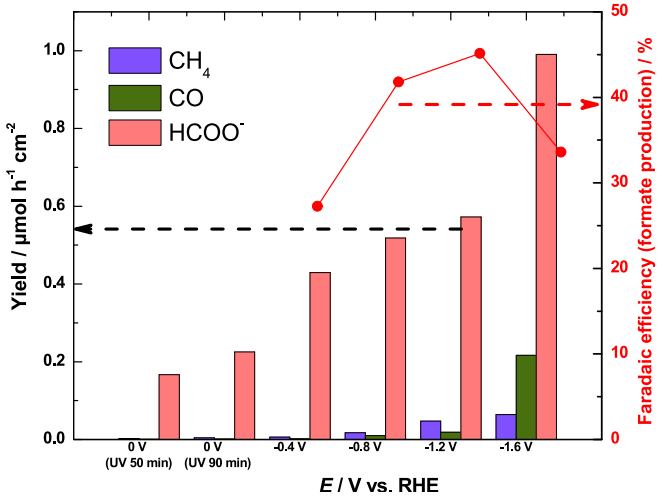

Fig. 4. Differential yields and Faradaic efficiencies of CO_2RR products of photo- and photoelectrocatalysis.

2.3. *In-situ ATR-FTIR spectroscopy studies*

To probe the real-time processes occurring on the TiO_2-DTF photocathode surface during the CO_2 reduction process, *in-situ* attenuated total reflection Fourier-transform infrared (ATR-FTIR) spectroscopy under both photochemical and photoelectrochemical conditions was conducted. *In-situ* ATR-FTIR spectra provide real-time evidence of the role of UV light in CO_2 adsorption and reduction. It is widely recognized that the interaction of species on the surface of TiO_2 is triggered by UV irradiation [66]. However, the interaction process, kinetics, and the influence of potential are not thoroughly understood. Therefore, the initial objective was to monitor the dynamics of adsorption and transformation of species on the TiO_2-DTF over varying durations of UV irradiation and applied potentials. As an initial step, it was crucial to attain a steady-state condition of the TiO_2 surface in contact with the solution. Achieving this steady state was essential for subsequent investigations into the impact of applied potential on the ongoing reactions. Without reaching this steady state, it would have been impossible to distinguish the effects of continuous UV irradiation from those of electrochemical processes.

Fig. 5a shows that upon the application of UV irradiation, the first bands to emerge are those around 1390 cm^{-1} and 1620 cm^{-1}, corresponding to the symmetric ν_s(COO) and asymmetric ν_{as}(COO) stretching of —COO^-, respectively. The emergence of these bands upon UV illumination indicates the light activation of CO_2 on the TiO_2 surface. The frequency shifts, $\Delta\nu$(COO) = (ν_{as}(COO)–ν_s(COO)), is around 230 cm^{-1} indicating a monodentate coordination of COO^- to the surface of TiO_2 [67]. Also, the sharp band quickly rising with UV irradiation duration around 1230 cm^{-1} is attributed to the bending of C—O bonds that are monodentately attached to surface TiO_2 surfaces [68]. These, in turn, indicate the formation of formate over time while its intensity increases as the TiO_2 surface becomes activated [66]. The progressive increase in the intensity of these bands over time (Fig. 5a) suggests that light not only enhances CO_2 adsorption but also facilitates the formation of reaction intermediates such as COOH* and HCOO*. Additional bands begin to appear after more than 30 min of UV irradiation. These bands can be roughly categorized into three groups. The first group consists of weak bands in the 2700–2800 cm^{-1} region, associated with C—H stretching modes, confirming gradual activation of the surface towards the formation of formate over time.

The second group consists of bands that are strongly linked to the

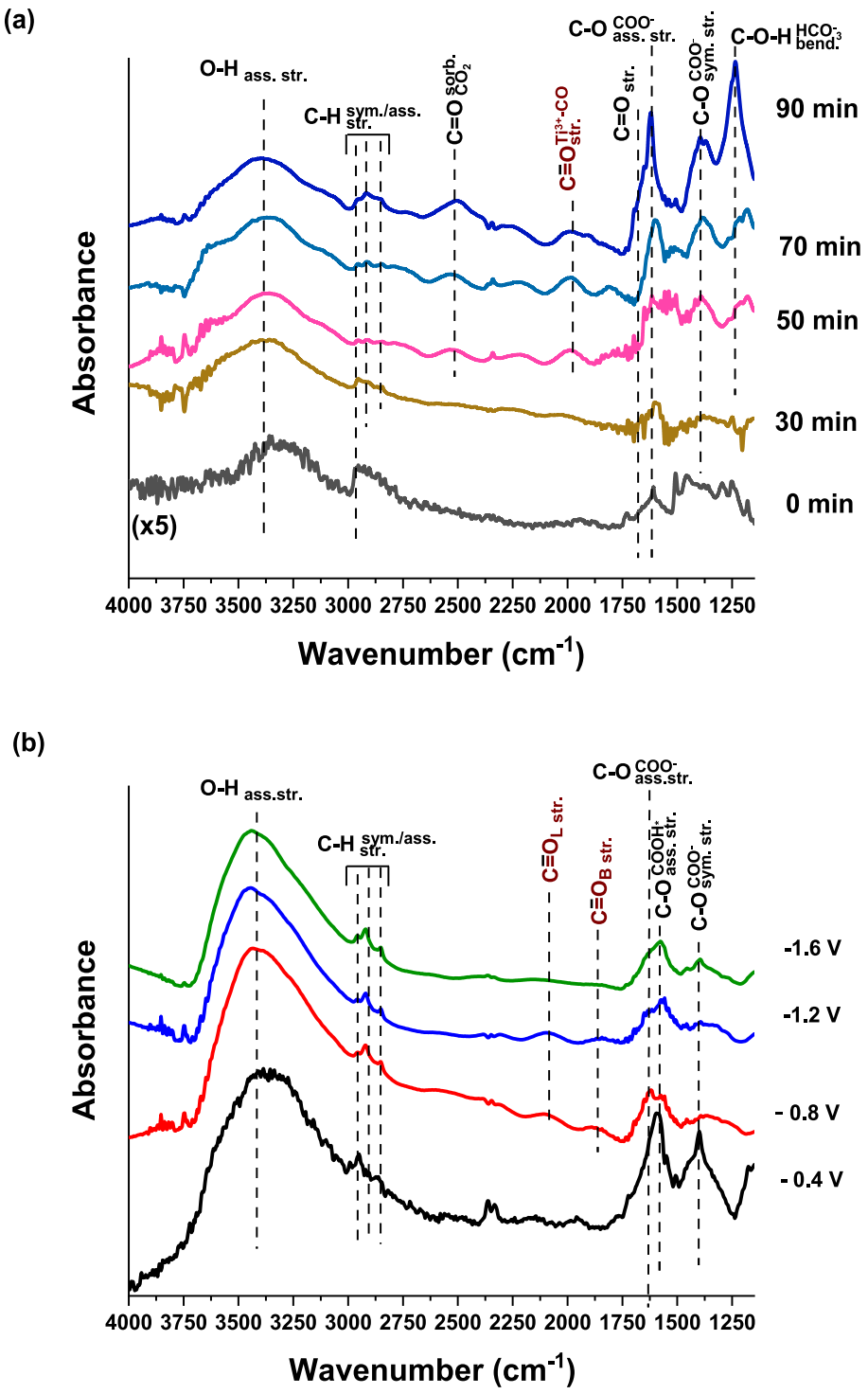

Fig. 5. *In-situ* ATR-FTIR spectra during photoactivation (a) under varying time periods without applied potential, and (b) with different applied potentials.

adsorption of CO_2-related species. Among these bands, the shoulder around 1700 cm^{-1} is broader and shows pronounced dependence on the duration of UV treatment. According to Wang et al., it can be attributed to C═O [69]. Also, the weak, sharp band around 2500 cm^{-1} is attributed to the stretching of C═O bonds. [70,71] The intensity increase of these bands aligns well with a recent study [72], which suggests that bicarbonate and carbonate species play a significant role during CO_2 conversion on the catalyst surface in a water solution.

And thirdly a weak, broad band around 1980 cm^{-1} is associated with the stretching of C≡O bonds in CO attached to Ti^{3+} atom [73]. The band is weak and does not exhibit significant growth over time, while bands related to bicarbonate ions and —COO^- species increase in intensity with the duration of IR treatment. After 90 min, they become the most prominent in the spectrum. This suggests that on a pure TiO_2 surface under UV treatment without an applied potential, the limiting step of the CO_2 reduction process is likely the proton-electron transfer to adsorbed bicarbonate ions, while the adsorption process itself occurs with relatively high efficiency. Additionally, as discussed earlier [66], UV irradiation plays a major role in activating the TiO_2 surface for enhanced adsorption of CO_2-related species from the solution. In general, under

UV-irradiation alone the spectra are dominated by water and CO_2-related species. The yield of products of CO_2 reduction under UV-irradiation without the applied potential is rather low, which is in good agreement with the results of product analysis described in previous section (Fig. 4).

Application of potential (Fig. 5b) dramatically changes the pattern of adsorption on the TiO_2 surface in the region below 1700 cm^{-1}, while the other part of spectra remains similar. The application of cathodic potential (Fig. 5b) further intensifies these bands, highlighting the synergistic effect of light and potential in driving CO_2 reduction. Main changes are linked with the shift from CO_2-related adsorbed species to CO_2 reduction products. The sharp C—O—H bending band around 1230 cm^{-1} linked to HCO_3 species disappears, others are either absent or fully convoluted with more intensive C—O stretching bands of COOH* and COO^- species (1575 and 1620 cm^{-1}) [74]. These features could also arise from formate accumulation both at the surface of the electrode and within the electrolyte. Furthermore, a band of short-living CO_2^- intermediate product becomes visible around 1690 cm^{-1} [68], indicating intensive reduction process on the TiO_2 surface.

Despite the proven influence of the cathodic potential on the production of $HCOO^-$ (as shown in Fig. 4), a general trend observed is that as the cathodic potential diminishes, the intensity of bands related to COO— decreases, indicating reduced adsorption despite the increase in products. This trend may be attributed to the repulsion effect of the cathodic potential due to the dipole moment of the adsorbates [75,76]. Conversely, the peaks of C—H in the 2700–2800 cm^{-1} region, whose relative peak intensities increase with the cathodic potential, align with the product analysis of Fig. 4, indicating the formation of CH_4.

The consistency between the ATR-FTIR results (on germanium substrates) and the electrochemical product analysis (on GC electrodes) demonstrates that the observed reaction mechanism and selectivity are intrinsic to the TiO_2 films. The primary product, formate, is not typically associated with GC electrodes under similar conditions, further confirming that the catalytic activity originates from the defect-rich TiO_2. Additionally, under UV illumination, the photoconductive properties of TiO_2 dominate the electrochemical response, rendering any potential effects of exposed glassy carbon negligible.

2.4. *Theoretical modeling of CO_2RR to C1 products via different pathways*

Theoretical calculations were performed to understand the details of the mechanism of CO_2RR on the anatase TiO_2 (1 0 1) surface after inducing Ti^{3+} defect with one oxygen vacancy (see SI for details of calculations, Fig. S5). The optimal electrocatalyst for CO_2 reduction reaction is typically identified through computational screening based on various criteria such as high selectivity, high activity, and strong chemisorption of CO_2 molecules [77]. The initial and critical step of CO_2RR is the adsorption of CO_2 onto the surface of the catalyst. Our analysis reveals that the synergistic interaction between Ti^{3+} and oxygen vacancy defects creates unique active sites that fundamentally enhance CO_2 activation. At these dual-active sites, Ti^{3+} centers facilitate electron transfer to the carbon atom of CO_2, while adjacent Ov sites provide optimal binding configurations for oxygen atoms, enabling efficient charge redistribution at the interface.

CO_2 adsorption is the rate-determining step of CO_2RR, with a free energy of 1.19 eV on the anatase TiO_2 (1 0 1) facet. However, after inducing the Ti^{3+} defect, the energy barriers of CO_2 adsorption on the anatase TiO_2 (1 0 1) surface are significantly reduced to 0.77 eV, due to the transfer of charges from the C-atom of CO_2 to the O-atoms of CO_2. These findings suggest that Ti^{3+} defective surfaces can improve CO_2 adsorption and, thus, enhance CO_2RR.

In the context of CO_2 reduction reactions, the presence of surface defects significantly influences reaction pathways and product distribution. While a broad set of C1 products can be generated, the formation of C2 products occurs rarely over atomic dispersion electro-catalysts owing to the lack of favorable binding sites for C—C coupling. The defect-mediated activation proceeds through stabilized intermediates, with COOH formation requiring only 0.23 eV and HCOO generation becoming favorable at −0.49 eV**.** These reaction pathways to C1 products are illustrated in Fig. 6a, while the Gibbs free energy diagrams for the three categories pathways, namely 2, 6, and 8 electron pathways to C1 products are depicted in Fig. 6b–d in the case of anatase TiO_2 (1 0 1) facet and Fig. 7a-c in the case of anatase TiO_2 (1 0 1) facet after inducing Ti^{3+}-defect with one oxygen vacancy. This analysis demonstrates how surface defects control both the reaction barriers and product selectivity through their influence on intermediate stability.

The main CO_2RR products via 2 electron pathways are CO and HCOOH. Fig. 6b, Fig. 7a and Table S4 show that CO_2RR to CO proceeds through $CO_2 \rightarrow COOH^* \rightarrow CO^* \rightarrow CO$. To activate the reaction, a Gibbs free energy of $\Delta G = 1.19$ eV is required to form COOH* intermediate on the anatase TiO_2 (1 0 1) surface, which decreases to $\Delta G = 0.77$ eV after inducing a Ti^{3+}-defect. The $COOH^* \rightarrow CO^*$ step has a favorable ΔG of 0.02 eV, while the ΔG for CO desorption is about −0.16 eV, which is more favorable than hydrogenation to form HCO* ($\Delta G = 0.15$ eV) or COH* ($\Delta G = 1.60$ eV) for anatase TiO_2(1 0 1) surface with a Ti^{3+}-defect. The CO desorption step is the potential limiting step for CO due to the stable adsorption of CO on the Ti^{3+} defect on the anatase TiO_2 (1 0 1) surface. Afterwards, for HCOOH generation, there are two possible reaction pathways: $CO_2 \rightarrow COOH^* \rightarrow HCOOH^* \rightarrow HCOOH$ (COOH pathway) and $CO_2 \rightarrow HCOO^* \rightarrow HCOOH^* \rightarrow HCOOH$ (HCOO pathway). The formation of COOH* requires a Gibbs free energy of about 0.77 eV, followed by hydrogenation at the C atom of COOH* with a $\Delta G = 0.23$ eV. The desorption of HCOOH is the energetically favorable process with a ΔG of −0.18 eV after inducing the Ti^{3+} defect. The initial activation of CO_2 to form HCOO* is easier than to form COOH* with a $\Delta G = -0.49$ eV for anatase TiO_2(1 0 1) surface with a Ti^{3+}-defect in contrast to the anatase TiO_2 (1 0 1) surface. However, the following $HCOO^* \rightarrow HCOOH^*$ step is more difficult for the anatase TiO_2(1 0 1) surface with a Ti^{3+}-defect than the anatase TiO_2 (1 0 1) surface with a ΔG of 1.02 eV. Thus, CO_2RR to HCOOH would proceed along the COOH pathway rather than the HCOO pathway, and the $CO_2 \rightarrow COOH^*$ step is the potential limiting step. In summary, CO_2RR via the two-electron pathway would yield HCOOH along the COOH pathway rather than CO with a relatively low Gibbs free energy of 0.23 eV on the anatase TiO_2 (1 0 1) surface slab after inducing a Ti^{3+}-defect.

Figs. 6c and 7b depict the reaction pathways of CO_2RR to CH_3OH via a six-electron pathway on the anatase TiO_2 (1 0 1) surface, both before and after inducing a Ti^{3+} defect. Once CO* is formed, there are two possible pathways for the hydrogenation of CO*: one at the C side to form HCO*, and the other at the O side to form COH*. The HCO* formation step is favorable with a ΔG of 0.15 eV, while the COH* formation step is difficult with a ΔG of 1.60 eV. The lower reaction free energy indicates that the hydrogenation of CO* is more likely to attack the C atom to form the HCO* intermediate. For the further hydrogenation of HCO*, both the O and C sides are taken into consideration. The $HCO^* \rightarrow HCHO^*$ step requires a ΔG of −0.33 eV, while the $HCO^* \rightarrow CHOH^*$ step requires a ΔG of 1.16 eV. Thus, CO_2RR tends to proceed along the $CHO^* \rightarrow HCHO^*$ step. The following hydrogenation at the C and O sides of HCHO* to form CH_2OH^* and CH_3O^* are both favorable with ΔG of 1.38 and −1.09 eV, respectively. For the next reaction of CH_2OH^*, a proton would attack C to form CH_3OH^* with a ΔG of −1.47 eV, followed by the desorption of CH_3OH with a ΔG of 0.08 eV. For the next reaction of CH_3O^*, a proton would attack O to form CH_3OH^* with a ΔG of 1.00 eV, which is 2.47 eV higher than that in the $CH_2OH^* \rightarrow CH_3OH^*$ step. Thus, CO_2RR after HCHO* formation tends to proceed via the CH_2OH^* intermediate. To summarize, CO_2RR to CH_3OH prefers to proceed along the following pathway: $CO2 \rightarrow COOH^* \rightarrow CO^* \rightarrow CHO^* \rightarrow HCHO^* \rightarrow CH_2OH^* \rightarrow CH_3OH^* \rightarrow CH_3OH$, and the largest ΔG required is 1.38 eV.

Additionally, CO_2 can be converted to methane (CH_4) through an eight-electron reaction pathway. The reaction-free energy diagrams for CH_4 generation are illustrated in Figs. 6d and 7c. The initial 6-electron

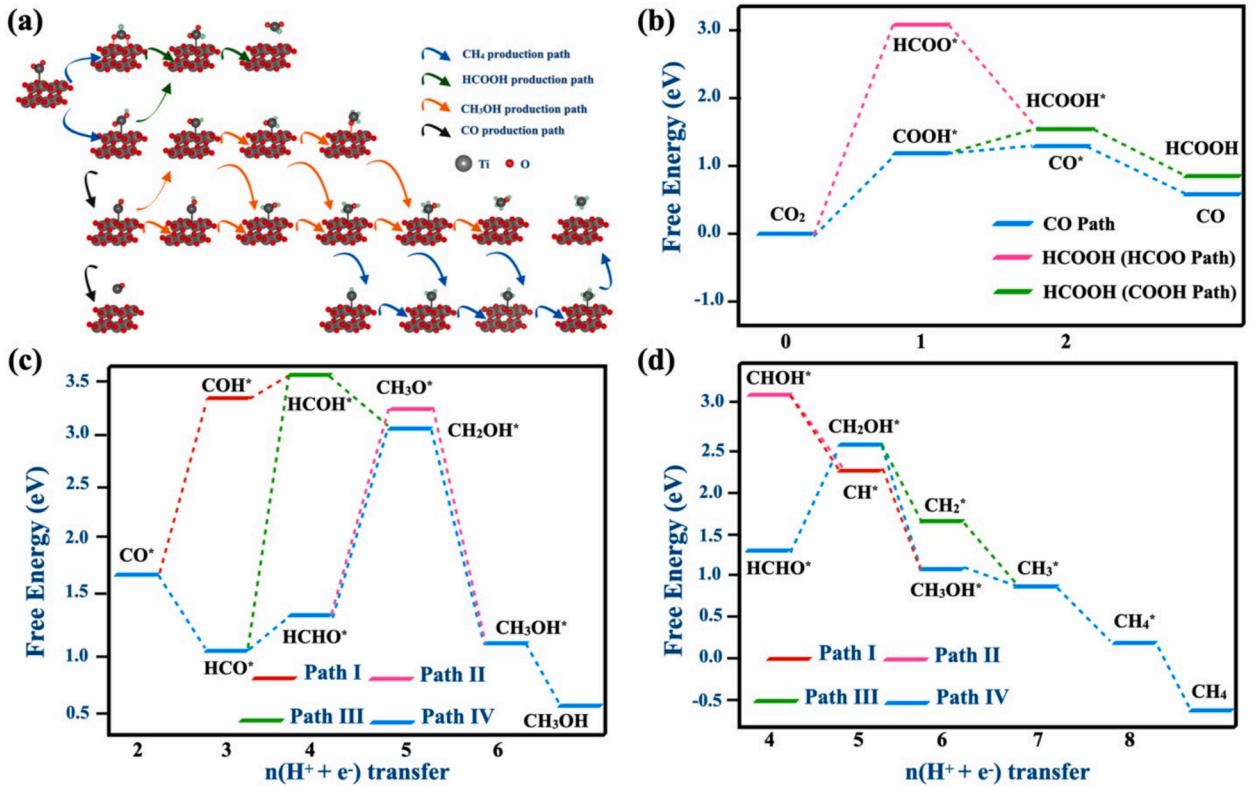

Fig. 6. (a) Detailed pathways of CO_2RR via a two-electron pathway to CO and HCOOH, via a six-electron pathway to CH_3OH, and an eight-electron pathway to CH_4. Free energy diagram of CO_2RR to (b) CO and HCOOH, (c) CH_3OH, and (d) CH_4 and corresponding intermediate configurations on anatase TiO_2 (1 0 1) surface slab at U = 0 V vs. RHE.

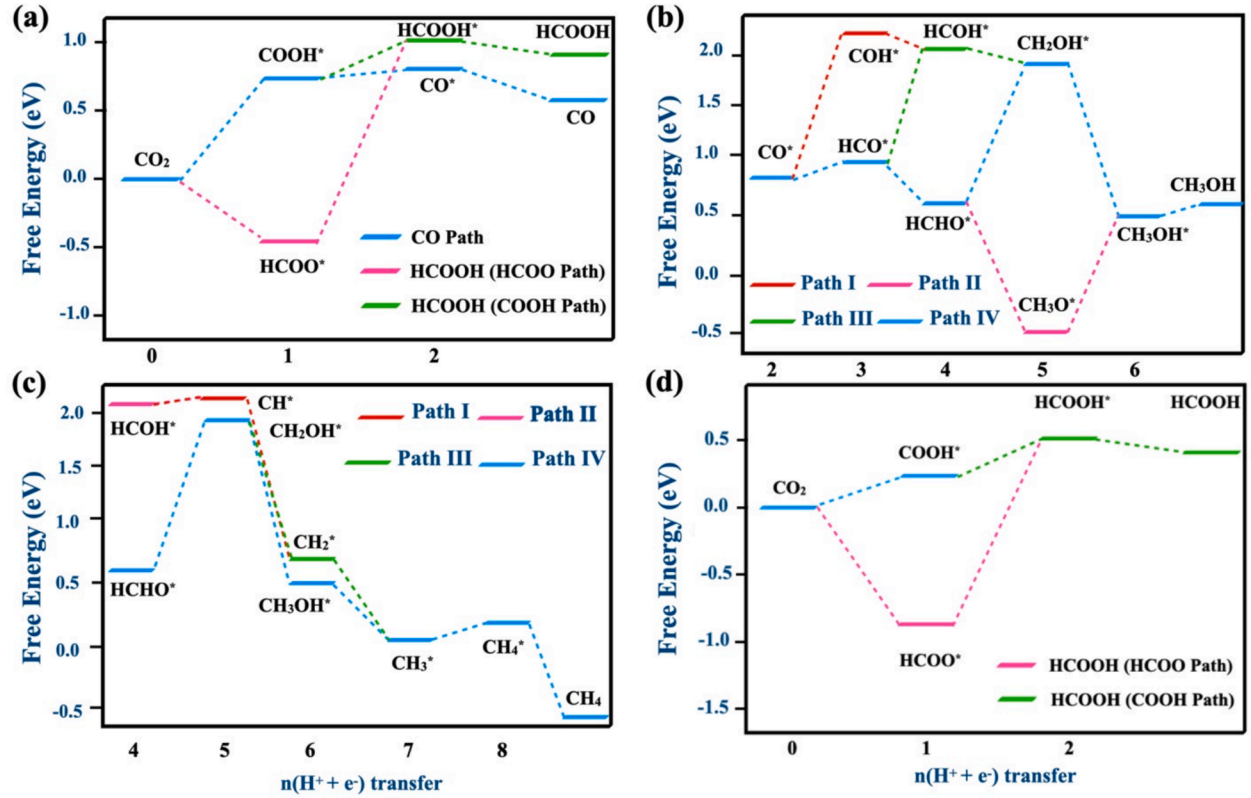

Fig. 7. (a) Free energy diagram of CO_2RR to (b) CO and HCOOH, (c) CH_3OH, and (d) CH_4 and corresponding intermediate configurations on anatase TiO_2 (1 0 1) surface after inducing Ti^{3+}-defect with one oxygen vacancy. (d) Free energy diagram of CO_2RR to HCOOH on anatase TiO_2(1 0 1) surface after inducing Ti^{3+}-defect at U = −0.4 V.

transfer steps in the CH_4 generation process are the same as those in the CH_3OH generation process. CO_2 reduction reaction tends to proceed along the pathway of $CO_2 \rightarrow COOH^* \rightarrow CO^* \rightarrow CHO^* \rightarrow HCHO^* \rightarrow CH_2OH^* \rightarrow CH_3OH^*$, and the largest free energy change is 1.38 eV. After the formation of CH_3OH^*, there are two downhill steps along $CH_3OH^* \rightarrow CH_3^*$ and $CH_4^* \rightarrow CH_4$, as well as a slight uphill step along $CH_3^* \rightarrow CH_4^*$. In the methane generation process, the $HCHO^* \rightarrow CH_2OH^*$ step requires the largest Gibbs free energy of about 1.38 eV, indicating that it is the potential limiting step in CH_4 generation. This suggests that CH_4 and CH_3OH compete with each other in CO_2RR on the anatase TiO_2 (1 0 1) surface after inducing the Ti^{3+} defect. A similar situation is observed in the case of the anatase TiO_2 (1 0 1) surface, with a potential limiting step of about 1.15 eV. Moreover, there are alternative reaction pathways for CH_4 generation. After the formation of CHOH*, in addition to hydrogenation at the C-atom, a proton can interact with the O-atom of CHOH* to form CH* with a Gibbs free energy of about 0.03 eV. CH_2^* is the possible reaction intermediate from CH_2OH^* or CH* for the next electron-transfer step. In conclusion, CO_2RR to CH_4 follows the pathway of $CO_2 \rightarrow COOH^* \rightarrow CO^* \rightarrow CHO^* \rightarrow HCHO^* \rightarrow CH_2OH^* \rightarrow CH_3OH^* \rightarrow CH_3^* \rightarrow CH_4^* \rightarrow CH_4$, and the largest free energy is 1.38 eV. To compare the selectivity of C1 products across different CO_2RR systems, we conducted a comparative analysis of limiting potentials (UL) for CO, HCOOH, CH_3OH, and CH_4, as illustrated in Fig. S6.

To obtain further insight into the reactivity of anatase TiO_2 (1 0 1) facet with Ti^{3+} defect in CO_2RR, the Gibbs free energy profiles for the synthesis of HCOOH under electrical potential were analysed and presented. The analysis was conducted at three distinct electrode potentials: U = −0.4, −1.2, and −1.6 V vs. RHE, preset by conditions of the photoelectrocatalytic experiment. Fig. 7d and Fig. S6(a, b) illustrate the calculated Gibbs free energy profiles under light irradiation conditions. It can be clearly noticed that the free energy changes associated with all steps involving proton-electron pairs are interrelated, as governed by the Gibbs free energy change (ΔG). The depicted free energy diagram clearly demonstrates a downhill trend for each step involved in the CO_2RR via the two-electron pathway leading to HCOOH formation in the case of U = −1.6 V vs. RHE potential, compared with uphill trend in the case of U = −0.4 V vs. RHE potential and near flat pathway in the case of U = −1.2 V vs. RHE. This downhill trend signifies that each reaction proceeds spontaneously, as the free energy decreases throughout the pathway.

The comparison between the product analysis, *in-situ* ATR-FTIR, and DFT calculations reveals valuable mechanistic insights into CO_2 photoelectroreduction on TiO_2 surfaces. In experiments, the increase in the favourability of the HCOOH* intermediate state with the application of cathodic potential was observed. The key distinction between photocatalytic and electro-photocatalytic processes on TiO_2 surfaces lies in their product outcomes: while photocatalysis typically yields CO with minor CH_4 amounts, applying cathodic potential shifts the process towards formate synthesis.

In recent works, the formation of $HCOO^-$ was considered improbable due to high desorption energy [78,79]; results of *in-situ* ATR-FTIR and DFT modelling in this study suggest that formation kinetics rather than desorption dynamics may be the primary limiting factor in formate production. In the case of UV-irradiation alone, the IR adsorption bands of CO_2-related species (mostly HCO_3^-) are intensified. However, the formation of products is hampered even for two-electron processes, confirming the suggestion that $CO_2 \rightarrow COOH^*$ is a limiting stage of the reduction process. The emergence of intensive peaks corresponding to CO_2 reduction products upon applying potential signifies the onset of intensive reduction via electron transfer. With the increase of potential, electron transfer becomes energetically favourable, and the process becomes limited by another stage, arguably desorption. On the other hand, the presence of CH_4 as the minor product with the absence of methanol, which should precede methane formation, can be explained by the high desorption energy of methanol from the TiO_2 surface [80]. Interestingly, the same work predicts the formation of CH_4 from bidentately bound CO [80], which was observed in our investigation under applied potential (Fig. 7d, and Fig. S6a, b).

In-situ ATR-FTIR spectroscopy captured the dynamic formation of reaction intermediates, such as $HCOO^-$ and $COOH^-$, on the TiO_2-DTF surface, strongly supporting the proposed mechanism of CO_2 reduction to formate. The presence of Ti^{3+} defects and oxygen vacancies, identified by XPS, is consistent with the high catalytic efficiency observed. These experimental results are further validated by DFT calculations, which confirm that defect-induced electronic modifications enhance CO_2 adsorption and activation.

3. Conclusion

This work offers a thorough examination of highly defective ultrathin TiO_2 films (TiO_2-DTF) as photoelectrocatalysts for CO_2 reduction. By manipulating TiO_2 film thickness and surface defect concentration, it was shown that the photoelectrocatalytic efficiency of TiO_2-DTF in CO_2 reduction can be significantly enhanced. Both experimental findings and theoretical modeling indicate that surface defects such as Ti^{3+} and oxygen vacancies play a crucial role in enhancing catalytic activity. Specifically, under UV light irradiation, the presence of these defects promotes CO_2 adsorption on the anatase TiO_2 (1 0 1) surface. Application of electrical potential leads to enhancement of both yield and selectivity of the formate production. The achieved Faradaic efficiencies of 45 % demonstrate the excellent performance of TiO_2-DTF as a low-cost and single-component catalyst material.

CRediT authorship contribution statement

Mahsa Amiri: Writing – original draft, Investigation, Formal analysis, Data curation, Conceptualization. **Majid Ahmadi:** Writing – review & editing, Methodology, Formal analysis, Conceptualization. **Nabil Khossossi:** Methodology, Investigation, Formal analysis, Data curation. **Prasad Gonugunta:** Methodology, Investigation, Formal analysis, Data curation. **Khatereh Roohi:** Methodology, Investigation, Formal analysis, Data curation. **Bart Kooi:** Methodology, Investigation, Formal analysis, Data curation. **Mahinder Ramdin:** Methodology, Investigation, Formal analysis, Data curation. **Prasaanth Ravi Anusuyadevi:** Methodology, Investigation, Formal analysis, Data curation. **Tanel Tätte:** Supervision. **Nadezda Kongi:** Writing – review & editing, Validation, Supervision, Project administration, Investigation, Funding acquisition, Formal analysis, Data curation, Conceptualization. **Alexander Vanetsev:** Writing – review & editing, Writing – original draft, Validation, Supervision, Methodology, Investigation, Formal analysis, Data curation, Conceptualization. **Poulumi Dey:** Writing – original draft, Methodology, Investigation, Formal analysis, Data curation, Conceptualization. **Peyman Taheri:** Writing – review & editing, Visualization, Supervision, Investigation, Data curation.

Declaration of competing interest

The authors declare that they have no known competing financial interests or personal relationships that could have appeared to influence the work reported in this paper.

Acknowledgement

This work was supported by the Estonian Research Council (PRG629, PSG250), European Union and Ministry of Education and Research (TEM-TA55), and by the Estonian Ministry of Education and Research (TK210). This work was facilitated by NWO Domain Science for the use of supercomputer facilities. The authors also acknowledge the use of DelftBlue supercomputer, provided by Delft High Performance Computing Center (https://www.tudelft.nl/dhpc).

Appendix A. Supplementary data

Supplementary data to this article can be found online at https://doi.org/10.1016/j.jcat.2025.116022.

Data availability

Data will be made available on request.

References

[1] X. Li, J. Yu, M. Jaroniec, X. Chen, Cocatalysts for selective photoreduction of CO_2 into solar fuels, Chem. Rev. 119 (6) (2019) 3962–4179, https://doi.org/10.1021/acs.chemrev.8b00400.

[2] S. Solomon, G.-K. Plattner, R. Knutti, P. Friedlingstein, Irreversible climate change due to carbon dioxide emissions, Proc. Natl. Acad. Sci. 106 (6) (2009) 1704–1709, https://doi.org/10.1073/pnas.0812721106.

[3] F.M. Mota, D.H. Kim, From CO_2 methanation to ambitious long-chain hydrocarbons: alternative fuels paving the path to sustainability, Chem. Soc. Rev. 48 (1) (2019) 205–259, https://doi.org/10.1039/C8CS00527C.

[4] W. Tu, Y. Zhou, Z. Zou, Photocatalytic conversion of CO2 into renewable hydrocarbon fuels: state-of-the-art accomplishment, challenges, and prospects, Adv. Mater. 26 (27) (2014) 4607–4626, https://doi.org/10.1002/adma.201400087.

[5] M.-Y. Lee, K.T. Park, W. Lee, H. Lim, Y. Kwon, S. Kang, Current achievements and the future direction of electrochemical CO_2 reduction: a short review, Crit. Rev. Environ. Sci. Technol. 50 (8) (2020) 769–815, https://doi.org/10.1080/10643389.2019.1631991.

[6] X. Chang, T. Wang, J. Gong, CO_2 photo-reduction: insights into CO_2 activation and reaction on surfaces of photocatalysts, Energy Environ. Sci. 9 (7) (2016) 2177–2196, https://doi.org/10.1039/C6EE00383D.

[7] N.S. Lewis, D.G. Nocera, Powering the planet: chemical challenges in solar energy utilization, Proc. Natl. Acad. Sci. 103 (43) (2006) 15729–15735, https://doi.org/10.1073/pnas.060339510.

[8] G.A. Olah, A. Goeppert, G.K.S. Prakash, Chemical recycling of carbon dioxide to methanol and dimethyl ether: from greenhouse gas to renewable, environmentally carbon neutral fuels and synthetic hydrocarbons, J. Org. Chem. 74 (2) (2009) 487–498, https://doi.org/10.1021/jo801260f.

[9] M. Ozkan, A. Shiner, N. Kongi, T.A. Hatton, S. Oldham, E. Sanders, Electrochemical direct air capture and direct ocean capture: the next frontier in carbon removal, Chem 10 (1) (2024) 3–6, https://doi.org/10.1016/j.chempr.2023.12.015.

[10] J. Antonio Abarca, G. Díaz-Sainz, I. Merino-Garcia, A. Irabien, J. Albo, Photoelectrochemical CO_2 electrolyzers: from photoelectrode fabrication to reactor configuration, J. Energy Chem. 85 (2023) 455–480, https://doi.org/10.1016/j.jechem.2023.06.032.

[11] L.B. Maia, I. Moura, J.J.G. Moura, Carbon dioxide utilisation—the formate route, Enzymes Solving Humankind's Probl, Nat. Artif. Syst. Health, Agric. Environ. Energy (2021) 29–81, https://doi.org/10.1007/978-3-030-58315-6_2.

[12] G. Díaz-Sainz, M. Alvarez-Guerra, B. Ávila-Bolívar, J. Solla-Gullón, V. Montiel, A. Irabien, Improving trade-offs in the figures of merit of gas-phase single-pass continuous CO_2 electrocatalytic reduction to formate, Chem. Eng. J. 405 (2021) 126965, https://doi.org/10.1016/j.cej.2020.126965.

[13] B. Ávila-Bolívar, R. Cepitis, M. Alam, J.-M. Assafrei, K. Ping, J. Aruväli, A. Kikas, V. Kisand, S. Vlassov, M. Käärik, J. Leis, V. Ivaništšev, P. Starkov, V. Montiel, J. Solla-Gullón, N. Kongi, CO_2 reduction to formate on an affordable bismuth metal-organic framework based catalyst, J. CO_2 Util. 59 (2022) 101937, https://doi.org/10.1016/j.jcou.2022.101937.

[14] I. Merino-Garcia, L. Tinat, J. Albo, M. Alvarez-Guerra, A. Irabien, O. Durupthy, V. Vivier, C.M. Sánchez-Sánchez, Continuous electroconversion of CO_2 into formate using 2 Nm Tin oxide nanoparticles, Appl. Catal. B 297 (2021) 120447, https://doi.org/10.1016/j.apcatb.2021.120447.

[15] A. Senocrate, C. Battaglia, Electrochemical CO_2 reduction at room temperature: status and perspectives, J. Storage Mater. 36 (2021) 102373, https://doi.org/10.1016/j.est.2021.102373.

[16] J. Albo, M. Alvarez-Guerra, A. Irabien, Electro-, photo-, and photoelectro-chemical reduction of CO_2, in: Heterogeneous Catalysts, John Wiley & Sons, Ltd, 2021, pp. 649–669, https://doi.org/10.1002/9783527813599.ch36.

[17] C. Wang, Z. Sun, Y. Zheng, Y.H. Hu, Recent progress in visible light photocatalytic conversion of carbon dioxide, J. Mater. Chem. A 7 (3) (2019) 865–887, https://doi.org/10.1039/C8TA09865D.

[18] S.K. Cushing, F. Meng, J. Zhang, B. Ding, C.K. Chen, C.-J. Chen, R.-S. Liu, A. D. Bristow, J. Bright, P. Zheng, N. Wu, Effects of defects on photocatalytic activity of hydrogen-treated titanium oxide nanobelts, ACS Catal. 7 (3) (2017) 1742–1748, https://doi.org/10.1021/acscatal.6b02177.

[19] C. Xu, P.R. Anusuyadevi, C. Aymonier, R. Luque, S. Marre, Nanostructured materials for photocatalysis, Chem. Soc. Rev. 48 (14) (2019) 3868–3902, https://doi.org/10.1039/C9CS00102F.

[20] S. Xie, Q. Zhang, G. Liu, Y. Wang, Photocatalytic and photoelectrocatalytic reduction of CO_2 using heterogeneous catalysts with controlled nanostructures, Chem. Commun. 52 (1) (2016) 35–59, https://doi.org/10.1039/C5CC07613G.

[21] I. Merino-Garcia, S. Castro, A. Irabien, I. Hernández, V. Rodríguez, R. Camarillo, J. Rincón, J. Albo, Efficient photoelectrochemical conversion of CO_2 to ethylene and methanol using a Cu cathode and TiO_2 nanoparticles synthesized in supercritical medium as photoanode, J. Environ. Chem. Eng. 10 (3) (2022) 107441, https://doi.org/10.1016/j.jece.2022.107441.

[22] Y. Boyjoo, Y. Jin, H. Li, G. Zhao, H. Guo, J. Liu, Nanoengineering of photocatalytic electrode materials toward net zero emissions, Cell Rep. Phys. Sci. 4 (5) (2023) 101391, https://doi.org/10.1016/j.xcrp.2023.101391.

[23] S. Palmas, L. Mais, M. Mascia, A. Vacca, Trend in using TiO_2 nanotubes as photoelectrodes in PEC processes for wastewater treatment, Curr. Opin. Electrochem. 28 (2021) 100699, https://doi.org/10.1016/j.coelec.2021.100699.

[24] I. Dundar, A. Mere, V. Mikli, M. Krunks, I. Oja Acik, Thickness effect on photocatalytic activity of TiO_2 thin films fabricated by ultrasonic spray pyrolysis, Catalysts 10 (9) (2020) 1058, https://doi.org/10.3390/catal10091058.

[25] S. Zavatski, E. Neilande, H. Bandarenka, A. Popov, S. Piskunov, D. Bocharov, Density functional theory for doped TiO_2: current research strategies and advancements, Nanotechnology 35 (19) (2024) 192001, https://doi.org/10.1088/1361-6528/ad272e.

[26] T. Berger, D. Monllor-Satoca, M. Jankulovska, T. Lana-Villarreal, R. Gómez, The electrochemistry of nanostructured titanium dioxide electrodes, ChemPhysChem 13 (12) (2012) 2824–2875, https://doi.org/10.1002/cphc.201200073.

[27] X. Yu, X. Han, Z. Zhao, J. Zhang, W. Guo, C. Pan, A. Li, H. Liu, Z. Lin Wang, Hierarchical TiO_2 nanowire/graphite fiber photoelectrocatalysis setup powered by a wind-driven nanogenerator: a highly efficient photoelectrocatalytic device entirely based on renewable energy, Nano Energy 11 (2015) 19–27, https://doi.org/10.1016/j.nanoen.2014.09.024.

[28] W. Siripala, A. Ivanovskaya, T.F. Jaramillo, S.-H. Baeck, E.W. McFarland, A Cu_2O/TiO_2 heterojunction thin film cathode for photoelectrocatalysis, Sol. Energy Mater. Sol. Cells 77 (3) (2003) 229–237, https://doi.org/10.1016/S0927-0248(02)00343-4.

[29] J. Zheng, F. Hu, E. Han, Z. Pan, S. Zhang, Y. Li, P. Qin, H. Wang, P. Li, H. Yin, Interaction between InP and SnO_2 on TiO_2 nanotubes for photoelectrocatalytic reduction of CO_2, Colloids Surf. A Physicochem. Eng. Asp. 575 (2019) 329–335, https://doi.org/10.1016/j.colsurfa.2019.05.016.

[30] L. Wang, Y. Wei, R. Fang, J. Wang, X. Yu, J. Chen, H. Jing, Photoelectrocatalytic CO_2 reduction to ethanol via graphite-supported and functionalized TiO_2 nanowires photocathode, J. Photochem. Photobiol. A Chem. 391 (2020) 112368, https://doi.org/10.1016/j.jphotochem.2020.112368.

[31] K. Wiranarongkorn, K. Eamsiri, Y.-S. Chen, A. Arpornwichanop, A comprehensive review of electrochemical reduction of CO_2 to methanol: technical and design aspects, J. CO_2 Util. 71 (2023) 102477, https://doi.org/10.1016/j.jcou.2023.102477.

[32] R. Konta, T. Ishii, H. Kato, A. Kudo, Photocatalytic activities of noble metal ion doped $SrTiO_3$ under visible light irradiation, J. Phys. Chem. B 108 (26) (2004) 8992–8995, https://doi.org/10.1021/jp049556p.

[33] C.-Y. Wu, Y.-L. Lee, Y.-S. Lo, C.-J. Lin, C.-H. Wu, Thickness-dependent photocatalytic performance of nanocrystalline TiO_2 thin films prepared by sol–gel spin coating, Appl. Surf. Sci. 280 (2013) 737–744, https://doi.org/10.1016/j.apsusc.2013.05.053.

[34] S. Mondal, D. Basak, Defect controlled tuning of the ratio of ultraviolet to visible light emission in TiO_2 thin films, J. Lumin. 179 (2016) 480–486, https://doi.org/10.1016/j.jlumin.2016.07.046.

[35] M.J. Torralvo, J. Sanz, I. Sobrados, J. Soria, C. Garlisi, G. Palmisano, S. Çetinkaya, S. Yurdakal, V. Augugliaro, Anatase photocatalyst with supported low crystalline TiO_2: the influence of amorphous phase on the activity, Appl. Catal. B 221 (2018) 140–151, https://doi.org/10.1016/j.apcatb.2017.08.089.

[36] H. Zhang, W. Wang, H. Liu, R. Wang, Y. Chen, Z. Wang, Effects of TiO_2 film thickness on photovoltaic properties of dye-sensitized solar cell and its enhanced performance by graphene combination, Mater. Res. Bull. 49 (2014) 126–131, https://doi.org/10.1016/j.materresbull.2013.08.058.

[37] J.-Y. Liu, X.-Q. Gong, R. Li, H. Shi, S.B. Cronin, A.N. Alexandrova, (Photo) Electrocatalytic CO_2 reduction at the defective anatase TiO_2 (1 0 1) surface, ACS Catal. 10 (7) (2020) 4048–4058, https://doi.org/10.1021/acscatal.0c00947.

[38] S.A. Rawool, K.K. Yadav, V. Polshettiwar, Defective TiO_2 for photocatalytic CO_2 conversion to fuels and chemicals, Chem. Sci. 12 (12) (2021) 4267–4299, https://doi.org/10.1039/D0SC06451C.

[39] J. Wang, R. Guo, Z. Bi, X. Chen, X. Hu, W. Pan, A review on TiO_{2-x}-based materials for photocatalytic CO_2 reduction, Nanoscale (2022), https://doi.org/10.1039/D2NR02527B.

[40] S. Doeuff, M. Henry, C. Sanchez, J. Livage, Hydrolysis of titanium alkoxides: modification of the molecular precursor by acetic acid, J. Non Cryst. Solids 89 (1) (1987) 206–216, https://doi.org/10.1016/S0022-3093(87)80333-2.

[41] B.E. Al-Jumaili, Fabrication and photoresponsive characteristics of ZnO film for ultraviolet ZnO/porous Si photodetector: the effect of post-processing treatment, Opt. Mater. 133 (2022) 112897, https://doi.org/10.1016/j.optmat.2022.112897.

[42] L.-E. Mo, Z.-Q. Li, Y.-C. Ding, C. Gao, L.-H. Hu, Y. Huang, T. Hayat, A. Alsaedi, S.-Y. Dai, Facile synthesis of TiO_2 microspheres via solvothermal alcoholysis method for high performance dye-sensitized solar cells, Sol. Energy 177 (2019) 448–454, https://doi.org/10.1016/j.solener.2018.10.013.

[43] U. Diebold, T.E. Madey, TiO_2 by XPS, Surf. Sci. Spectra 4 (3) (1996) 227–231, https://doi.org/10.1116/1.1247794.

[44] S. Kang, R. Mauchauffé, Y.S. You, S.Y. Moon, Insights into the role of plasma in atmospheric pressure chemical vapor deposition of titanium dioxide thin films, Sci. Rep. 8 (1) (2018) 16684, https://doi.org/10.1038/s41598-018-35154-4.

[45] S.A. Abdullah, M.Z. Sahdan, N. Nafarizal, H. Saim, Z. Embong, C.H. Cik Rohaida, F. Adriyanto, Influence of substrate annealing on inducing Ti^{3+} and oxygen vacancy in TiO_2 thin films deposited via RF magnetron sputtering, Appl. Surf. Sci. 462 (2018) 575–582, https://doi.org/10.1016/j.apsusc.2018.08.137.

[46] Handbook of X-Ray Photoelectron Spectroscopy: A Reference Book of Standard Spectra for Identification and Interpretation of XPS Data, Update.; J.F. Moulder, J. Chastain (Eds.), Perkin-Elmer Corporation, Eden Prairie, Minn, 1992.
[47] W. Jiang, H. Loh, B.Q.L. Low, H. Zhu, J. Low, J.Z.X. Heng, K.Y. Tang, Z. Li, X. J. Loh, E. Ye, Role of oxygen vacancy in metal oxides for photocatalytic CO_2 reduction, Appl. Catal. B 321 (2023) 122079, https://doi.org/10.1016/j.apcatb.2022.122079.
[48] F. Gunkel, D.V. Christensen, Y.Z. Chen, N. Pryds, Oxygen vacancies: the (in)visible friend of oxide electronics, Appl. Phys. Lett. 116 (12) (2020) 120505, https://doi.org/10.1063/1.5143309.
[49] R. Fang, M. He, H. Huang, Q. Feng, J. Ji, Y. Zhan, D.Y.C. Leung, W. Zhao, Effect of redox state of ag on indoor formaldehyde degradation over Ag/TiO_2 catalyst at room temperature, Chemosphere 213 (2018) 235–243, https://doi.org/10.1016/j.chemosphere.2018.09.019.
[50] A. Khlyustova, N. Sirotkin, T. Kusova, A. Kraev, V. Titov, A. Agafonov, Doped TiO_2: the effect of doping elements on photocatalytic activity, Mater. Adv. 1 (5) (2020) 1193–1201, https://doi.org/10.1039/D0MA00171F.
[51] X. Zou, Y. Yang, H. Chen, X.-L. Shi, G. Suo, X. Ye, L. Zhang, X. Hou, L. Feng, Z.-G. Chen, Tuning wall thickness of TiO_2 microtubes for an enhanced photocatalytic activity with thickness-dependent charge separation efficiency, J. Colloid Interface Sci. 579 (2020) 463–469, https://doi.org/10.1016/j.jcis.2020.06.081.
[52] S. Bakhtiarnia, S. Sheibani, A. Billard, H. Sun, E. Aubry, M.A.P. Yazdi, Enhanced photocatalytic activity of sputter-deposited nanoporous $BiVO_4$ thin films by controlling film thickness, J. Alloy. Compd. 879 (2021) 160463, https://doi.org/10.1016/j.jallcom.2021.160463.
[53] K. Jiang, Y. Huang, G. Zeng, F.M. Toma, W.A.I.I.I. Goddard, A.T. Bell, Effects of surface roughness on the electrochemical reduction of CO_2 over Cu, ACS Energy Lett. 5 (4) (2020) 1206–1214, https://doi.org/10.1021/acsenergylett.0c00482.
[54] M. Coto, S.C. Troughton, P. Knight, R. Joshi, R. Francis, R.V. Kumar, T.W. Clyne, Optimization of the microstructure of TiO_2 photocatalytic surfaces created by plasma electrolytic oxidation of titanium substrates, Surf. Coat. Technol. 411 (2021) 127000, https://doi.org/10.1016/j.surfcoat.2021.127000.
[55] Z.S. Hosseini, F. Haghparast, A.A. Masoudi, A. Mortezaali, Enhanced visible photocatalytic performance of un-doped TiO_2 nanoparticles thin films through modifying the substrate surface roughness, Mater. Chem. Phys. 279 (2022) 125530, https://doi.org/10.1016/j.matchemphys.2021.125530.
[56] A. Kumar, V.K. Saxena, R. Thangavel, B.K. Nandi, A dual effect of surface roughness and photocatalysis of crystalline TiO_2-thin film for self-cleaning application on a photovoltaic covering glass, Mater. Chem. Phys. 289 (2022) 126427, https://doi.org/10.1016/j.matchemphys.2022.126427.
[57] A. Corma, H. Garcia, Photocatalytic reduction of CO_2 for fuel production: possibilities and challenges, J. Catal. 308 (2013) 168–175, https://doi.org/10.1016/j.jcat.2013.06.008.
[58] I. Sher, E. Sher, A novel internal combustion engine utilizing internal hydrogen production for improved efficiency – a theoretical concept, Int. J. Hydrogen Energy 39 (33) (2014) 19182–19186, https://doi.org/10.1016/j.ijhydene.2014.09.079.
[59] D. Seo, A. Ma, T. Kwon, K.M. Nam, Tailoring co-catalysts on Si photocathode for efficient photoelectrochemical CO_2 reduction: recent progress and prospect of deposition methods, Inorg. Chem. Front. 11 (2024) 998–1018, https://doi.org/10.1039/D3QI02293E.
[60] S. Liu, Z. Guo, Y. Yang, P. Wu, Z. Li, K. Wang, H. Zhang, H. Li, S. Yang, Cobalt-doped CdS quantum dots enhanced photoelectroreduction of CO_2 to formic acid with high selectivity, Environ. Chem. Lett. (2024) 1–8, https://doi.org/10.1007/s10311-023-01691-2.
[61] W.J. Dong, I.A. Navid, Y. Xiao, J.W. Lim, J.-L. Lee, Z. Mi, CuS-decorated GaN nanowires on silicon photocathodes for converting CO_2 mixture gas to HCOOH, J. Am. Chem. Soc. 143 (27) (2021) 10099–10107, https://doi.org/10.1021/jacs.1c02139.
[62] Q. Gong, P. Ding, M. Xu, X. Zhu, M. Wang, J. Deng, Q. Ma, N. Han, Y. Zhu, J. Lu, Z. Feng, Y. Li, W. Zhou, Y. Li, Structural defects on converted bismuth oxide nanotubes enable highly active electrocatalysis of carbon dioxide reduction, Nat. Commun. 10 (1) (2019) 2807, https://doi.org/10.1038/s41467-019-10819-4.
[63] S.K. Choi, U. Kang, S. Lee, D.J. Ham, S.M. Ji, H. Park, Sn-coupled p-Si nanowire arrays for solar formate production from CO_2, Adv. Energy Mater. 4 (11) (2014) 1301614, https://doi.org/10.1002/aenm.201301614.
[64] B. Zhou, X. Kong, S. Vanka, S. Cheng, N. Pant, S. Chu, P. Ghamari, Y. Wang, G. Botton, H. Cuo, Z. Mi, A GaN:Sn nanoarchitecture integrated on a silicon platform for converting CO_2 to HCOOH by photoelectrocatalysis, Energy Environ. Sci. 12 (9) (2019) 2842–2848, https://doi.org/10.1039/C9EE01339C.
[65] C. Li, X. Zhou, Q. Zhang, Y. Xue, Z. Kuang, H. Zhao, C.-Y. Mou, H. Chen, Construction of heterostructured Sn/TiO_2/Si photocathode for efficient photoelectrochemical CO_2 reduction, ChemSusChem 15 (8) (2022) e202200188, https://doi.org/10.1002/cssc.202200188.
[66] R. Nakamura, A. Imanishi, K. Murakoshi, Y. Nakato, In situ FTIR studies of primary intermediates of photocatalytic reactions on nanocrystalline TiO_2 films in contact with aqueous solutions, J. Am. Chem. Soc. 125 (24) (2003) 7443–7450, https://doi.org/10.1021/ja029503q.
[67] G. Shustak, A.J. Domb, D. Mandler, Preparation and characterization of N-alkanoic acid self-assembled monolayers adsorbed on 316L stainless steel, Langmuir 20 (18) (2004) 7499–7506, https://doi.org/10.1021/la036470z.
[68] L. Liu, H. Zhao, J.M. Andino, Y. Li, Photocatalytic CO_2 reduction with H_2O on TiO_2 nanocrystals: comparison of anatase, rutile, and brookite polymorphs and exploration of surface chemistry, ACS Catal 2 (8) (2012) 1817–1828, https://doi.org/10.1021/cs300273q.
[69] Z.-W. Wang, Q. Wan, Y.-Z. Shi, H. Wang, Y.-Y. Kang, S.-Y. Zhu, S. Lin, L. Wu, Selective photocatalytic reduction CO_2 to CH_4 on ultrathin TiO_2 nanosheet via coordination activation, Appl. Catal. B 288 (2021) 120000, https://doi.org/10.1016/j.apcatb.2021.120000.
[70] L.-F. Liao, C.-F. Lien, D.-L. Shieh, M.-T. Chen, J.-L. Lin, FTIR study of adsorption and photoassisted oxygen isotopic exchange of carbon monoxide, carbon dioxide, carbonate, and formate on TiO_2, J. Phys. Chem. B 106 (43) (2002) 11240–11245, https://doi.org/10.1021/jp0211988.
[71] Y. Katayama, L. Giordano, R.R. Rao, J. Hwang, H. Muroyama, T. Matsui, K. Eguchi, Y. Shao-Horn, Surface (electro) chemistry of CO_2 on Pt surface: an in situ surface-enhanced infrared absorption spectroscopy study, J. Phys. Chem. C 122 (23) (2018) 12341–12349, https://doi.org/10.1021/acs.jpcc.8b03556.
[72] M. Dunwell, X. Yang, B.P. Setzler, J. Anibal, Y. Yan, B. Xu, Examination of near-electrode concentration gradients and kinetic impacts on the electrochemical reduction of CO_2 using surface-enhanced infrared spectroscopy, ACS Catal 8 (5) (2018) 3999–4008, https://doi.org/10.1021/acscatal.8b01032.
[73] E.R. Corson, R. Kas, R. Kostecki, J.J. Urban, W.A. Smith, B.D. McCloskey, R. Kortlever, In situ ATR–SEIRAS of carbon dioxide reduction at a plasmonic silver cathode, J. Am. Chem. Soc. 142 (27) (2020) 11750–11762, https://doi.org/10.1021/jacs.0c01953.
[74] S. Zhu, T. Li, W.-B. Cai, M. Shao, CO_2 electrochemical reduction as probed through infrared spectroscopy, ACS Energy Lett. 4 (3) (2019) 682–689, https://doi.org/10.1021/acsenergylett.8b02525.
[75] P. Taheri, K. Pohl, G. Grundmeier, J.R. Flores, F. Hannour, J.H.W. de Wit, J.M. C. Mol, H. Terryn, Effects of surface treatment and carboxylic acid and anhydride molecular dipole moments on the volta potential values of zinc surfaces, J. Phys. Chem. C 117 (4) (2013) 1712–1721, https://doi.org/10.1021/jp3096049.
[76] P. Taheri, J. Wielant, T. Hauffman, J.R. Flores, F. Hannour, J.H.W. de Wit, J.M. C. Mol, H. Terryn, A comparison of the interfacial bonding properties of carboxylic acid functional groups on zinc and iron substrates, Electrochim. Acta 56 (4) (2011) 1904–1911, https://doi.org/10.1016/j.electacta.2010.10.079.
[77] F. Lei, W. Liu, Y. Sun, J. Xu, K. Liu, L. Liang, T. Yao, B. Pan, S. Wei, Y. Xie, Metallic tin quantum sheets confined in graphene toward high-efficiency carbon dioxide electroreduction, Nat. Commun. 7 (1) (2016) 12697, https://doi.org/10.1038/ncomms12697.
[78] Y. Ji, Y. Luo, New mechanism for photocatalytic reduction of CO_2 on the anatase TiO_2 (1 0 1) surface: the essential role of oxygen vacancy, J. Am. Chem. Soc. 138 (49) (2016) 15896–15902, https://doi.org/10.1021/jacs.6b05695.
[79] Y. Ji, Y. Luo, Theoretical study on the mechanism of photoreduction of CO_2 to CH_4 on the anatase TiO_2(1 0 1) surface, ACS Catal. 6 (3) (2016) 2018–2025, https://doi.org/10.1021/acscatal.5b02694.
[80] J.-Y. Liu, X.-Q. Gong, A.N. Alexandrova, Mechanism of CO_2 photocatalytic reduction to methane and methanol on defected anatase TiO_2 (1 0 1): a density functional theory study, J. Phys. Chem. C 123 (6) (2019) 3505–3511, https://doi.org/10.1021/acs.jpcc.8b09539.